



Nonlinear temporal compression in multipass cells: theory

MARC HANNA,^{1,*} XAVIER DÉLEN,¹ LOIC LAVENU,^{1,2} FLORENT GUICHARD,² YOANN ZAOUTER,² FRÉDÉRIC DRUON,¹ AND PATRICK GEORGES¹

¹Laboratoire Charles Fabry, UMR 8501, Institut d'Optique, CNRS, Université Paris Saclay, 2 Avenue Augustin Fresnel, 91127 Palaiseau, France

²Amplitude Systèmes, 11 Avenue de Canteranne, Cité de la Photonique, 33600 Pessac, France

*Corresponding author: marc.hanna@institutoptique.fr

Received 20 March 2017; revised 3 May 2017; accepted 13 May 2017; posted 15 May 2017 (Doc. ID 290927); published 5 June 2017

The use of multipass cells as a way to spatially homogenize self-phase modulation and distribute its accumulation over the propagation distance is analyzed in detail, with the aim to perform nonlinear temporal compression. In addition to the insertion of nonlinear media at specific locations in the cell, as already demonstrated, we also propose to fill the cell with a noble gas, as is done in hollow capillary-based setups. This makes the accumulation of B -integral continuous rather than discrete. In this case, analytical estimates for the B -integral per round trip and scaling rules are provided as a function of cavity geometry and gas parameters. Then, three-dimensional numerical simulations are performed to assess the spatiotemporal couplings in the output beam in various conditions. This model is checked against experimental data presented in the literature, and used to predict our proposed scheme performance. We believe that these techniques constitute a promising way to allow temporal compression at energy levels beyond 10 mJ, where capillary-based setups are difficult to implement. © 2017 Optical Society of America

OCIS codes: (320.5520) Pulse compression; (320.7110) Ultrafast nonlinear optics; (190.4420) Nonlinear optics, transverse effects in.

<https://doi.org/10.1364/JOSAB.34.001340>

1. INTRODUCTION

Temporal compression of ultrashort pulses using self-phase modulation (SPM) and subsequent propagation in a negative dispersion optical setup is a standard tool in ultrafast optics. Nowadays, it is the most common way to access the few-cycle regime from standard Ti-Sa lasers [1,2] triggering the fascinating field of attosecond physics [3]. It is also commonly implemented at the output of high-power Yb-doped material-based lasers [4], which are otherwise limited by gain narrowing to pulse durations above 200 fs for fiber and 1 ps for YAG systems. This technique considerably widens the possible applications of available ultrafast laser systems.

SPM is generally carried out in a waveguide, thereby increasing the interaction length and circumventing the spatial manifestation of the Kerr effect. Indeed, when an ultrafast pulse propagates in a bulk material, the spatial Kerr effect causes quick beam degradation and spatiotemporal couplings, preventing the accumulation of large temporal nonlinear phases. Although there have been some attempts to use a single or several bulk SPM media [5] by carefully adjusting the input beam size and divergence, these experiments generally show that the parameter space for temporal compression while

avoiding space–time couplings and beam degradation is much reduced.

For waveguide-based temporal compression setups, operation below the critical power for self-focusing is compensated by a large interaction distance, allowing accumulation of large nonlinear phases. The nature of the waveguide must be adapted to the input pulse parameters, in particular, the input peak power. For input peak powers below the self-focusing threshold in silica, around 4 MW, silica fibers have been used successfully, e.g., to compress pulses with energies of the order of a few microjoules [6,7]. At higher energy levels, the nonlinear medium used is typically a gas-filled hollow waveguide, exhibiting a self-focusing power threshold 3 orders of magnitude higher than silica when a gas pressure around 1 bar is used. For pulse energies in the 1–100 μ J range, Kagome fibers with typical diameter of a few tens of microns have lately been successfully used [8,9], but the residual overlap of the optical mode with the thin silica struts featured in these fibers structure prevent further energy scaling. For pulse energies in the 100 μ J–10 mJ range, gas-filled dielectric hollow capillaries with typical diameters of a few hundreds of microns are routinely used [1,2]. The use of these structures is limited on the low-energy side by high losses

in small diameter capillaries, and on the high-energy side by the onset of ionization and the need of impractically long waveguides that must be maintained strictly straight to avoid losses [10].

Recently, a concept for using bulk SPM has been proposed and successfully applied to the compression of 37 μJ pulses at 375 W average power from 850 fs down to 170 fs [11]. It consists in using a multipass cell (MPC) in which bulk SPM media are inserted at specific locations. In a fashion similar to laser cavities [12,13] and regenerative amplifiers [14], the nonlinearity is therefore distributed over a large number of passes, and propagation in the cavity somehow plays the same spatial homogenizing role as a waveguide that can be naïvely seen as a string of successive lenses. As in waveguides, if the spatial phase induced by the Kerr effect can be neglected compared to spatial phases induced by propagation in the MPC over a round trip, the spatial effect is washed out, leaving only the desired temporal nonlinear phase. This is still valid when the peak power in the bulk medium exceeds the self-focusing threshold, provided the self-focusing distance is much larger than the medium length. This concept offers additional robustness compared to hollow waveguide implementations, being much less sensitive to pointing instabilities, offers additional control on the propagation through possible design of the dispersion and reflectivity of the mirrors, and its only limitations are related to optical damage threshold of the mirrors, bulk materials, and coatings, which can be engineered by cavity design.

In this paper, we first propose and analyze theoretically in detail what we believe is a novel scheme that consists in utilizing a MPC filled with a nonlinear gas instead of solid-state SPM media at discrete locations in the MPC. This idea was investigated in the case of plasma-induced spectral broadening [15], but not for SPM-induced broadening, to our knowledge. This introduces a number of benefits: it alleviates the need for dispersion management in the MPC caused by the bulk medium, results in a continuous rather than discrete distribution of SPM along the propagation, reduces the overall losses induced by optical interfaces, and generally allows scaling nonlinear temporal compression systems to higher pulse energies. Because the pulse propagates continuously in the nonlinear medium, the peak power must be kept below the self-focusing threshold, but this threshold can be adjusted using the gas pressure. For these gas-filled MPCs, we provide analytical expressions for the accumulated B -integral per round trip and energy-scaling considerations.

In the second part, we present a 3D numerical model of pulse propagation that is used to analyze in more detail both MPCs, including discrete bulk nonlinear media and gas-filled MPCs. This model is first validated against the experimental data presented in [11], and then used to predict the performance of temporal compression systems in different configurations. In particular, the model allows us to assess the spatiotemporal couplings induced by different MPC geometries and input pulse parameters. Finally, we conclude with the applicability of this technique for various laser systems and open the discussion to a possible more general use of MPCs incorporating nonlinearity.

2. ACCUMULATED B -INTEGRAL AND SCALING RULES FOR GAS-FILLED CAVITIES

A. MPC Geometry

The simple symmetric MPC geometry considered in this paper is shown in Fig. 1. It consists in two identical mirrors with radius of curvature R separated by a distance L . In this section, we consider that the MPC is filled with a nonlinear gas. We will think of this MPC exactly as a laser cavity, meaning that the input beam must be mode matched to satisfy steady-state operation, thereby leading to a constant B -integral per round trip. The pulses to be compressed should be fed to the MPC slightly off-axis using small mirrors to allow convenient in- and out-coupling, following the multipass geometry described in [16]. At fixed radius of curvature, as L is increased, several configurations appear. When L is small compared to R , the cavity waist radius w_0 is small as well as the beam radius on the mirror w_M . In this case, the cavity length is below twice the Rayleigh distance inside the cavity. When $R = L$, the cavity is confocal, corresponding to the largest waist w_0 at fixed R , and the beam propagates over exactly twice the Rayleigh distance inside the cavity. For values of L larger than R , and approaching the cavity stability limit $L = 2R$, the size of the waist w_0 decreases toward zero while the beam size on the mirrors w_M increases to infinity. The ratio of beam size on the mirror and beam size at the waist is given by $(w_M/w_0)^2 = 2R/(2R - L)$.

In terms of accumulation of the Kerr effect, the most distributed case is the small cavity case ($L < R$), where beam size changes are minimal across the cavity. However, this also corresponds to small beam sizes, and a very short cavity makes in- and out-coupling more difficult. In the confocal case, input and output coupling is not possible because beam locations on the mirrors reproduce after two round trips, forming a two-spot pattern on each mirror. Experimental implementations should therefore be slightly detuned from the confocal situation. An important aspect is the spatial homogenizing of the Kerr effect, where geometric intuition suggests that imaging situations should be avoided. For instance, cavities with lengths approaching the stability limit $L = 2R$ tend to concentrate the accumulation of the Kerr effect close to the cavity waist, and are close to the situation where this waist is reimaged onto itself over successive round trips. This situation is expected to be unfavorable in terms of spatial homogenizing. One of the keys of the spatial homogenizing function of the MPC is to accumulate nonlinear phase at positions along the beam that are far from being images of one another. This will be analyzed quantitatively in the simulations section.

B. Calculation of the B -Integral

We now evaluate analytically the B -integral accumulated along one MPC round trip. Given the fact that we seek to

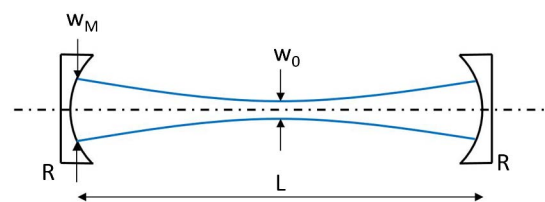


Fig. 1. Geometry of the symmetric two-mirror MPC.

homogenize the nonlinear phase over the beam section, we choose the definition used in guided-wave nonlinear optics:

$$B_{\text{roundtrip}} = 4 \frac{2\pi n_2 P_{\text{peak}}}{\lambda} \int_0^{L/2} \frac{1}{A_{\text{eff}}(z)} dz, \quad (1)$$

where n_2 is the nonlinear index of the gas, P_{peak} is the peak power assumed independent of the propagation distance in the absence of significant dispersion, λ is the central wavelength, and A_{eff} is the local effective area defined by $A_{\text{eff}} = \pi w^2(z)$ for a Gaussian beam. Modification of the beam size imparted by the spatial Kerr effect are not considered in this analysis. This assumption is valid at low nonlinearity levels, for which the beam width remains stationary over the successive round trips. Simulations performed in Section 3 show that it is the case for usable output beam, i.e., beams that exhibit low space-time couplings. The definition of Eq. (1) gives values that are equal to half the B -integral accumulated on-axis (corresponding to the maximum intensity), because of the Gaussian shape of the beam. It can be easily evaluated as a function of MPC parameters R and L and the threshold power for critical self-focusing $P_{\text{crit}} = \lambda^2/8n_2$:

$$B_{\text{roundtrip}} = \pi \frac{P_{\text{peak}}}{P_{\text{crit}}} \text{atan} \left(\sqrt{\frac{L}{2R-L}} \right). \quad (2)$$

This quantity is plotted as a function of resonator length for different radii of curvature in Fig. 2, showing that the B -integral increases monotonously as the MPC length is increased. This plot also highlights the fact that at fixed n_2 and input pulse parameters, the range of accessible B -integral per round trip does not depend much on the choice of the mirror radius of curvature. Finally, the cavity geometry fixes a proportionality constant between the ratio of input power to critical power and the B -integral per round trip. As an example, regardless of cavity length L , the use of a confocal cavity operated at an input power equal to $P_{\text{crit}}/2$ to ensure no catastrophic collapse of the beam fixes the B -integral per round trip to $\pi^2/8 \approx 1.23$ rad.

As a side note, for the most general stable two-mirror cavity with a waist w_0 located at $z = 0$ and mirrors with radii of curvature R_1 and R_2 located at positions z_1 and z_2 , it can be easily

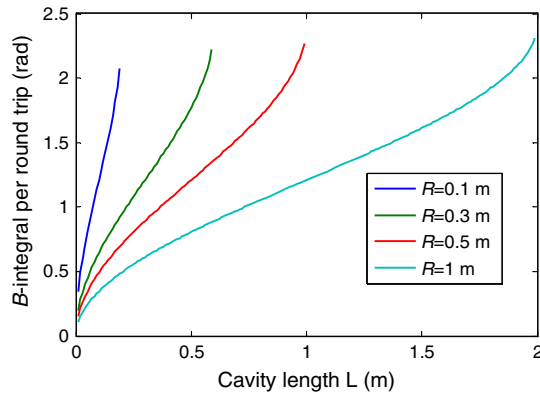


Fig. 2. B -integral per round trip as a function of MPC length and mirror radius of curvature for a peak power of $P_{\text{peak}} = 1.3$ GW at $\lambda = 1030$ nm and $n_2 = 5 \times 10^{-23}$ m²/W, corresponding to $P_{\text{peak}}/P_{\text{crit}} = 0.5$.

shown, following the same procedure as described above, that the B -integral per round trip is given by

$$B_{\text{roundtrip}} = \frac{\pi P_{\text{peak}}}{2 P_{\text{crit}}} \left(\text{atan} \frac{z_2}{z_R} - \text{atan} \frac{z_1}{z_R} \right). \quad (3)$$

This equation shows that the situation where $z_1, z_2 > +z_R$, corresponding to convex-concave cavities with beam sizes on the mirrors much larger than the beam waist (located outside of the cavity) induce a very small nonlinear phase per round trip at a fixed $P_{\text{peak}}/P_{\text{crit}}$ ratio. This finding justifies our choice to consider symmetric cavities, since keeping the waist inside the cavity leads to viable values of the accumulated nonlinear phase per round trip. Moreover, in such a cavity, the beam remains in the far field, which is not expected to mix the spatial components and homogenize the spatial Kerr effect. The next section is devoted to limitations of the gas-filled setup and scaling considerations.

C. Scaling Rules

We now address the question of the energy-scaling limits of this system. Two limitations are taken into account: optical damage on the MPC mirrors, defined by a damage threshold fluence J_d , and onset of ionization in the gas medium, defined by a limit peak intensity above which the ionization rate is too high to ensure proper operation of the MPC, I_{ion} . We restrict this analysis to symmetrical MPCs. We start by fixing the radius of curvature R of the mirrors, and determine the MPC lengths that are compatible with the input pulse energy E_{in} and duration $\Delta\tau$. The MPC length and beam size on the mirrors and at the waist are related by

$$L = \frac{2\pi^2 R w_M^4}{\pi^2 w_M^4 + \lambda^2 R^2}, \quad (4)$$

$$L = R \pm \sqrt{R^2 - \frac{4\pi^2 w_0^4}{\lambda^2}}. \quad (5)$$

The beam size is limited on the mirrors by the damage threshold to values satisfying $\pi w_M^2 > E_{\text{in}}/J_d$ and at the cavity waist to values satisfying $\pi w_0^2 > 2E_{\text{in}}/(I_{\text{ion}}\Delta\tau)$. At a fixed radius of curvature, the values of cavity lengths ensuring operation below the damage and ionization threshold are therefore given by

$$L > \frac{2RE_{\text{in}}^2}{E_{\text{in}}^2 + \lambda^2 R^2 J_d^2}, \quad (6)$$

$$L < R + \sqrt{R^2 - \frac{16E_{\text{in}}^2}{\lambda^2 \Delta\tau^2 I_{\text{ion}}^2}}, \quad L > R - \sqrt{R^2 - \frac{16E_{\text{in}}^2}{\lambda^2 \Delta\tau^2 I_{\text{ion}}^2}}. \quad (7)$$

To illustrate these limits, Fig. 3 displays the area in the (R, L) MPC parameters space that can be operated with input pulse parameters of $E_{\text{in}} = 500$ mJ and $\Delta\tau = 500$ fs, corresponding to possible future kilohertz high-energy Yb-based systems [17,18]. The value for the limit ionization intensity is 10^{14} W/cm², and the considered damage threshold is $J_d = 10$ J/cm². Ionization limits the operation to MPC lengths away from the stability edges, while damage on the mirror imposes a minimal MPC length. The typical distances needed to perform nonlinear compression of such a high-energy

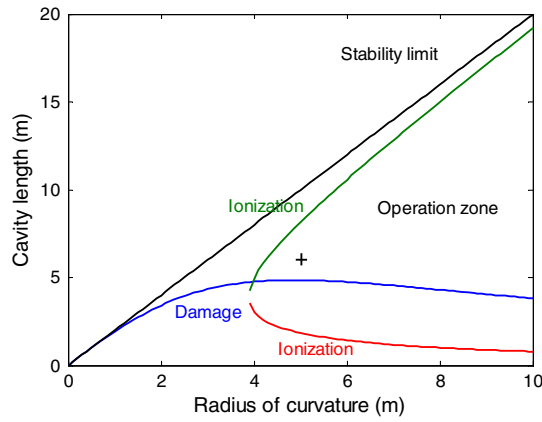


Fig. 3. Safe MPC operation zone for the following parameters: pulse energy 500 mJ, pulse duration 500 fs, ionization intensity 10^{14} W/cm², and damage threshold $J_d = 10$ J/cm². The cross indicates the operation point at which 3D simulations are performed in Section 3.

pulse are of the order of a few meters, indicating that experimental implementation is realistic.

We now examine the most important aspect of nonlinear compression in MPCs: how propagation allows spatial redistribution of the Kerr-induced phase, resulting in homogeneous, spatiotemporal couplings-free output beams. This requires the use of a numerical 3D propagation model, detailed in the next section.

3. NUMERICAL SIMULATIONS

A. Numerical Model

The model is based on a **symmetric** split-step Fourier algorithm accounting for linear effects such as diffraction and dispersion in the frequency domain, while the Kerr effect is modeled in the space–time domain. The linear complex envelope field propagation is calculated in the Fourier domain according to

$$E(\omega, f_x, f_y, z + dz) = E(\omega, f_x, f_y, z) \times \exp \left(ik(\omega) \sqrt{1 - \frac{4\pi^2}{k(\omega)^2} (f_x^2 + f_y^2) dz} \right), \quad (8)$$

where ω is the angular frequency, f_x and f_y are the transverse spatial frequencies, and z is the propagation distance. The quantity $k(\omega) = \omega n(\omega)/c$, where c is the speed of light in vacuum, is the wave vector, including dispersion of the local material. This dispersion is taken into account by using a Sellmeier equation describing the frequency dependence of the linear index for the material of interest, thereby accounting for all orders. Nonlinear propagation of the field is described in the space–time domain by the following equation:

$$E(t, x, y, z + dz) = E(t, x, y, z) \exp(ik_0 n_2 I(t, x, y, z) dz), \quad (9)$$

where t is time, x and y are transverse dimensions, k_0 is the wave vector at the central wavelength in vacuum, and

$I = 2c\epsilon_0 |E|^2$ is the local intensity. This model is applied with a grid size of $128 \times 128 \times 256$ in the space and time domains. The step sizes are adjusted in the space domain to cover the whole beam on the mirrors while providing sufficient definition at the waist. In the time domain, the step size is defined to accommodate the initial pulse duration together with the broadened output spectrum. In all cases, we verify that sampling is adequate by checking that the same results are obtained when increasing the number of points. Curved mirrors are modeled as simple quadratic phases in the space domain, with the possibility of adding a space-independent spectral phase to model chirped mirrors that can be used to compensate for material dispersion as in [11]. Although it can be easily taken into account, no losses were introduced in the model, since ultralow-loss mirrors and antireflection coatings are available. At the output of the cavity, a space-independent quadratic spectral phase is added and adjusted to optimize compression in the time domain. In summary, this model takes into account diffraction, dispersion to all orders, and the temporal and spatial manifestations of the instantaneous Kerr effect: SPM and self-focusing. The initial condition is Gaussian in space and time, and is matched to the fundamental spatial mode of the considered cavity. The model can be easily adapted to both the gas-filled and the bulk nonlinear medium MPC setups.

B. Test Case: Discrete Kerr Nonlinearity

We start by applying our model to the case described in [11]. The simulation parameters are matched to the experimental data reported: input pulse duration 850 fs, input pulse energy 30 μ J, mirror radius of curvature 350 mm, mirror dispersion -400 fs², MPC length 540 mm, number of round trips 18, and 13 mm-thick fused silica windows are added as nonlinear media at both ends of the MPC. In this case, SPM is taken into account only during propagation in silica, i.e., nonlinearity in air is supposed to be negligible.

The results are plotted in Fig. 4, showing excellent agreement with the experimental data obtained in [11]. The most remarkable feature of the output 160 fs compressed pulses (requiring the introduction of a group delay dispersion of -30000 fs²) is the excellent spectral and temporal homogeneity, as shown in Figs. 4(c) and 4(d). The on-axis value of the B -integral calculated using the simulation is 19 rad, matching quite well the estimated value reported in [11] of 5π . The appearance of a slight halo together with a decrease of the output beam size is visible on the output beam profile, indicating that the B -integral value per round trip of ~ 1 rad is at the limit of what can be done using this setup without causing spatiotemporal aberrations.

To clearly illustrate the homogenizing role of the cavity, Fig. 5 shows the spectrospatial profiles obtained above compared to the case of an identical pulse experiencing the same B -integral in a single plane, which is close to what happens in a single-stage bulk nonlinear compression system where the nonlinear crystal length is small compared to the Rayleigh range of the input collimated beam. The strong spectrospatial coupling obtained in this case is obvious, with a spectral broadening that directly depends on the transverse spatial intensity. In particular, the spectral broadening observed at the beam

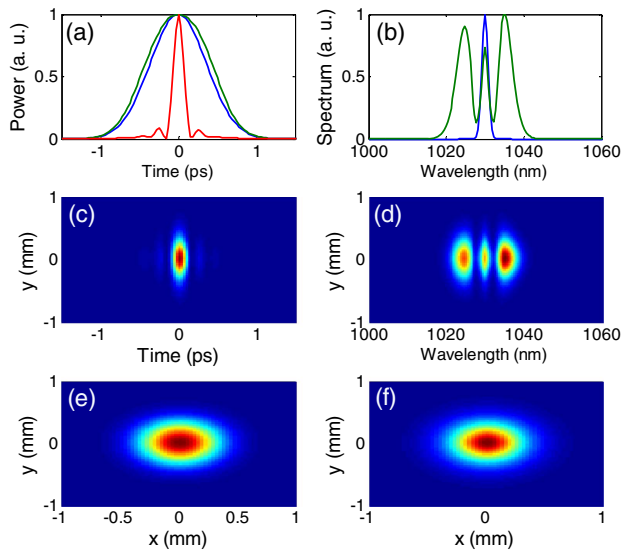


Fig. 4. Simulation results for parameters corresponding to [11] with input energy of 30 μJ . (a) Temporal profile at the input (blue) space integrated temporal profile at the output before (green) and after dispersion (red); (b) spectrum at the input (blue) and space-integrated spectrum at the output (green); (c) spatiotemporal profile of the compressed pulse; (d) spatio-spectral profile of the compressed pulse; (e) beam profile at the input; (f) time-integrated beam profile at the output.

center corresponds to twice the equivalent B -integral observed in the cavity case, while it is negligible at the beam edges because of the Gaussian spatial dependence of the intensity. In contrast, the cavity redistributes this nonlinear phase over the whole beam in a process similar to what happens in a waveguide, resulting in an effective area that halves the accumulated B -integral as described by Eq. (1).

The model is then run at an input energy of 40 μJ to reproduce the fast degradation observed in [11]. As seen in Fig. 6, the pulses cannot be compressed anymore, showing that our model captures the physics of the spatial homogenizing process at work in the cavities. The spectrum shown in Fig. 6(b) matches the reported experimental data in terms of general shape and width, but does not exactly reproduce it. This might be due to the fact that, in this energy range where a fast beam degradation occurs, the output pulse depends very sensitively on the input conditions (e.g., energy and pulse shape). Another

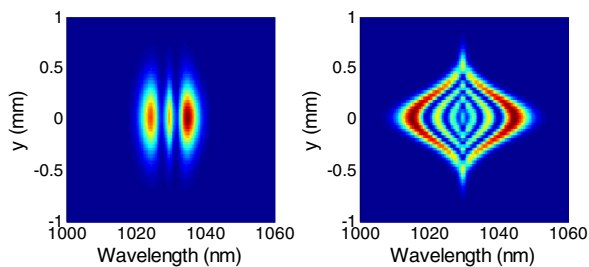


Fig. 5. Comparison of spatio-spectral profiles in the cavity case (left) and for a pulse accumulating the same on-axis B -integral in one plane (right).

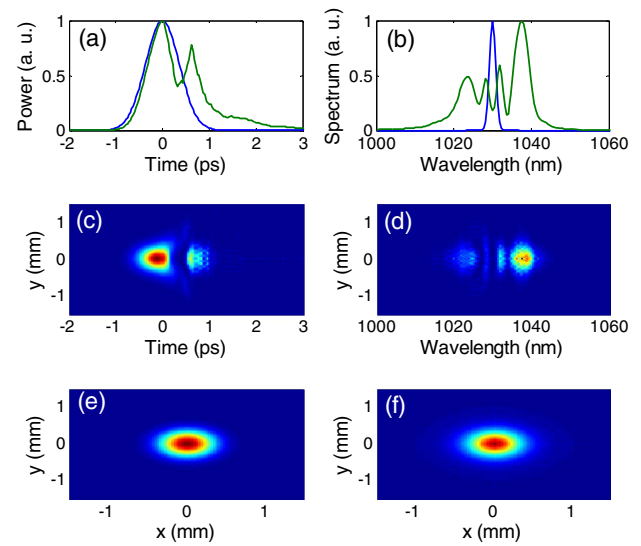


Fig. 6. Simulation results for parameters corresponding to [11] with input energy of 40 μJ . (a) Temporal profile at the input (blue) space integrated temporal profile at the output before dispersion (green); (b) spectrum at the input (blue) and space-integrated spectrum at the output (green); (c) spatiotemporal profile at the output of the cavity; (d) spatio-spectral profile at the output of the cavity; (e) beam profile at the input; (f) time-integrated-beam profile at the output.

possibility is that since there are significant space–time couplings, the exact procedure to measure the spectrum might have an impact on the result. Our interpretation of the temporal profile shown in Fig. 6(a) is as follows: the central, intense part of the pulse in time undergoes strong self-focusing and is radiated away from the beam center, as shown clearly in the spatiotemporal plot. Part of this halo can accumulate larger group delay, forming the delayed temporal wing and the interference structure observed in the trailing edge of the pulse.

To illustrate further the fact that our simulation captures the rapid beam quality degradation observed experimentally in the energy range 30–40 μJ , Fig. 7 (left) shows line-outs of the spatial profiles at the input and output of the cavity at 30 μJ and 40 μJ energy levels. It is clear that a significant fraction of the energy is shed in a wide halo at 40 μJ , as typically observed in nonlinear compression setups in single-stage bulk material. We also compute the M^2 parameter (averaged over time) at the output of the MPC as a function of input energy. Figure 7

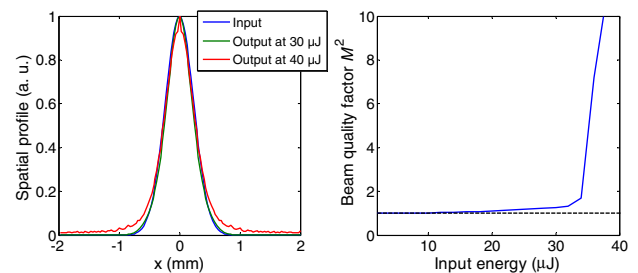


Fig. 7. Left: line-out of the beam profile at the input and output of the MPC for 30 μJ and 40 μJ energies. Right: output beam quality as a function of input pulse energy.

(right) displays clearly the fast beam quality degradation at around 35 μJ energy level, in good agreement with the experimentally observed data in [11].

C. Nonlinear Compression in Gas-Filled MPCs

We now apply our model to simulate the compression of a high-energy ultrashort Yb-doped fiber amplifier similar to the one described in [19] in a gas-filled MPC. The parameters are as follows: input pulse duration 150 fs, input pulse energy 200 μJ , mirror radius of curvature 300 mm, no mirror dispersion, cavity length 300 mm, number of round trips 20, and the nonlinear index in the cavity is $5 \times 10^{-23} \text{ m}^2/\text{W}$, corresponding to 1 bar of xenon or 5 bars of argon. Compared to the previous case, the energy is almost 1 order of magnitude larger while the initial pulse duration is much shorter, and the goal is to assess whether a gas-filled MPC can be used to access the few-cycle regime as described in [19] using a capillary, while providing robustness and convenient scaling to higher input energies. The parameters have been chosen in order to operate in the safe zone with respect to ionization and mirror damage, as explained above. Simulation results are plotted in Fig. 8, and show that the MPC allows pulse compression down to 11 fs, corresponding to 3.6 optical cycles at 1.03 μm , while preserving an excellent output beam quality. This technique therefore constitutes an extremely versatile architecture that can be used over a broad range of input parameters in terms of energy and pulse width.

To further explore energy scaling of this setup, the same model is now applied to input pulse parameters considered in Section 2.C corresponding to a future possible high-energy diode-pumped Yb:CaF₂-based system, i.e., $E_{\text{in}} = 500 \text{ mJ}$ and

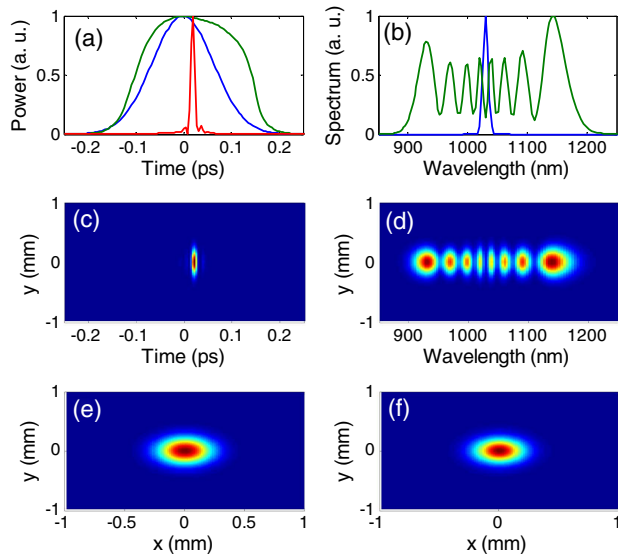


Fig. 8. Simulation results for parameters corresponding to a high-energy fiber amplifier. (a) Temporal profile at the input (blue) space-integrated temporal profile at the output before (green) and after dispersion (red); (b) spectrum at the input (blue) and space integrated spectrum at the output (green); (c) spatiotemporal profile of the compressed pulse; (d) spatio-spectral profile of the compressed pulse; (e) beam profile at the input; (f) time-integrated beam profile at the output.

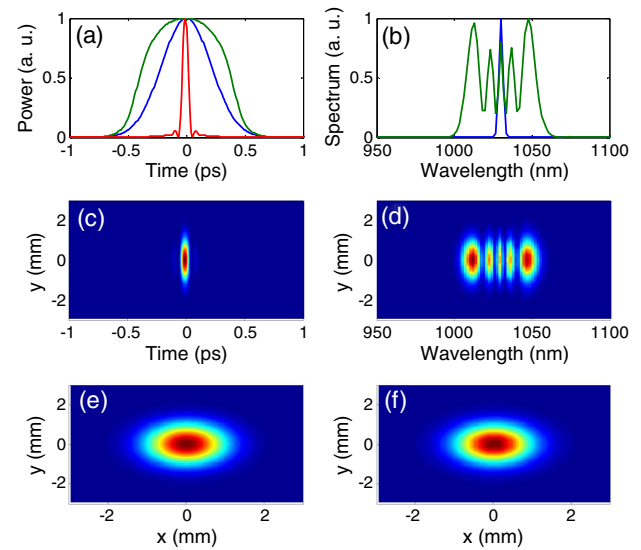


Fig. 9. Simulation results for parameters corresponding to a high-energy bulk Yb:CaF₂ system. (a) Temporal profile at the input (blue) space integrated temporal profile at the output before (green) and after dispersion (red); (b) spectrum at the input (blue) and space-integrated spectrum at the output (green); (c) spatiotemporal profile of the compressed pulse; (d) spatio-spectral profile of the compressed pulse; (e) beam profile at the input; (f) time-integrated beam profile at the output.

$\Delta\tau = 500 \text{ fs}$. As described in Fig. 3, avoiding ionization and mirror damage requires the use of meter-sized cavities, and we choose to model a 6 m-long MPC with mirror radius of curvature of 5 m, which is close to the confocal situation. In order to operate well below the self-focusing threshold in this case, the nonlinear index must be turned down to $5 \times 10^{-26} \text{ m}^2/\text{W}$, approximately corresponding to 50 mbars of neon. In this case, after propagation through 15 round trips, the output pulse exhibits good spatial quality and can be compressed down to 53 fs (Fig. 9), showing that the technique is in principle applicable to terawatt laser systems.

D. Influence of Cavity Geometry on Space-Time Couplings

To gain some more insight into the dependence of the performances of the setup to MPC parameters, and starting from the operation point described in Fig. 8 corresponding to a fiber amplifier, we now study the compression ratio and space-time couplings as a function of nonlinearity and cavity length at a fixed radius of curvature. We do not restrict the MPC geometries to realistic values that avoid mirror damage and ionization to fully explore the parameter space. In order to quantify the spatiotemporal couplings, we introduce a metric. The first step is to define the beam size $\Delta r(t)$ and divergence $\Delta f(t)$ as the square root of the second-order moments for $r = \sqrt{x^2 + y^2}$ and $f = \sqrt{f_x^2 + f_y^2}$, respectively, which are functions of time. We can then compute a time-dependent beam parameter product $\text{BPP}(t) = \Delta r(t)\Delta f(t)$. Our metric for the space-time couplings is then defined as the standard deviation of this BPP normalized by the average value of the BPP over time

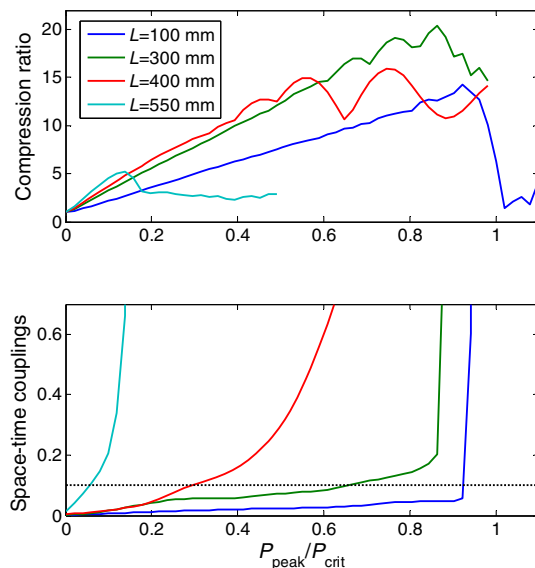


Fig. 10. Compression ratio (top) and space–time couplings (bottom) as a function of $P_{\text{peak}}/P_{\text{crit}}$ ratio for different MPC lengths with fixed radius of curvature $R = 300$ mm. The dashed line indicates $\text{STC} = 0.1$.

$\text{STC} = \sigma_{\text{BPP}}/\langle \text{BPP} \rangle$. In other words, when the beam quality is constant as a function of time, $\text{STC} = 0$, and this value increases as the spatial properties of the beam increasingly depend on the time value considered. An arbitrarily defined threshold value of STC below 0.1 indicates that spatial-properties are mostly time independent, resulting in a usable beam at the output.

Figure 10 shows the compression ratio, defined as the ratio of compressed peak power to input peak power, and space–time coupling metric as n_2 is increased (expressed by the ratio $P_{\text{peak}}/P_{\text{crit}}$), with other parameters kept equal to the situation of Fig. 8 (input energy 200 μJ , $R = 300$ mm, 20 round trips), for different MPC lengths $L = 100$ mm, $L = 300$ mm (confocal cavity), $L = 400$ mm, and $L = 550$ mm (close to the stability edge). For each value of n_2 , compression is optimized by adding a purely quadratic space-independent spectral phase at the output of the MPC. As expected from the analytical results, the compression ratio initially increases faster for longer MPCs as n_2 is increased because the accumulated B -integral per round trip is higher. However, the longest MPC, which is close to the concentric stability edge, induces fast increase of the space–time couplings, and it is not possible to compress the pulses with a ratio greater than 5. As mentioned earlier, this is in line with the intuitive picture that suggests that in this situation, the nonlinear phase is mostly accumulated at the beam waist, which is imaged onto itself after successive round trips, allowing the accumulation of aberrations rather than spatial homogenizing of SPM. The short and confocal MPCs both allow compression of the pulse by a factor of 10 to 15 while keeping low space–time couplings. The value of $P_{\text{peak}}/P_{\text{crit}}$ that corresponds to acceptable spatiotemporal couplings at the output decreases as the MPC length is increased. This can be understood by the fact that nonlinearity is increasingly localized at the waist as the MPC size is increased.

4. CONCLUSION

We study in detail the use of MPCs as a substitute for waveguides in nonlinear compression setups, presenting both analytical results for gas-filled MPCs and simulations that are applicable to both MPCs incorporating a bulk nonlinear medium and gas-filled MPCs. This technique is extremely versatile and can be applied to a large range of pulse energies and durations, offering a promising way to scale the output energies of such setups. Design rules and physical insight are provided as to how propagation spatially homogenizes the nonlinear phase, and what the viable operation points are.

These nonlinear cavities are somehow similar to fibers in the sense that linear and nonlinear effects are distributed. Although most of this paper concerns MPCs with almost no dispersion, the mirrors can be used to introduce a controllable amount of dispersion. This points toward operation regimes that are well-established in fibers, such as solitonic self-compression, parabolic regime, spectral compression, which all require controlled dispersion and nonlinearity. Most of these effects have indeed been observed in the case of cavities incorporating gain, but have not been used in passive MPCs to our knowledge. Other nonlinear effects such as the Raman effect could also be used. In the case of MPCs, the dispersion and nonlinearity are particularly easy to adjust, and various functions such as spectral filters can also easily be incorporated through mirror design. This suggests that a wide range of optical setups involving nonlinear optics in fibers can be used at much higher pulse energies using MPCs.

Funding. Agence Nationale de la Recherche (ANR) (ANR-10-LABX-0039, ANR-11-BS09-02801); Conseil Départemental de l'Essonne (SOPHIE).

REFERENCES

1. M. Nisoli, S. De Silvestri, O. Svelto, R. Szipöcs, K. Ferencz, C. Spielmann, S. Sartania, and F. Krausz, "Compression of high-energy laser pulses below 5 fs," *Opt. Lett.* **22**, 522–524 (1997).
2. J. Park, J.-H. Lee, and C. H. Nam, "Generation of 1.5 cycle 0.3 TW laser pulses using a hollow-fiber pulse compressor," *Opt. Lett.* **34**, 2342–2344 (2009).
3. F. Calegari, G. Sansone, S. Stagira, C. Vozzi, and M. Nisoli, "Advances in attosecond science," *J. Phys. B* **49**, 062001 (2016).
4. J. Rothhardt, S. Hädrich, A. Klenke, S. Demmler, A. Hoffmann, T. Gotschall, T. Eidam, M. Krebs, J. Limpert, and A. Tünnermann, "53 W average power few-cycle fiber laser system generating soft x rays up to the water window," *Opt. Lett.* **39**, 5224–5227 (2014).
5. M. Seidel, G. Arisholm, J. Brons, V. Pervak, and O. Pronin, "All solid-state spectral broadening: an average and peak power scalable method for compression of ultrashort pulses," *Opt. Express* **24**, 9412–9428 (2016).
6. T. Südmeyer, F. Brunner, E. Innerhofer, R. Paschotta, K. Furusawa, J. C. Baggett, T. M. Monro, D. J. Richardson, and U. Keller, "Nonlinear femtosecond pulse compression at high average power levels by use of a large-mode-area holey fiber," *Opt. Lett.* **28**, 1951–1953 (2003).
7. C. Jocher, T. Eidam, S. Hädrich, J. Limpert, and A. Tünnermann, "Sub 25 fs pulses from solid-core nonlinear compression stage at 250 W of average power," *Opt. Lett.* **37**, 4407–4409 (2012).
8. F. Emaury, C. Fourcade Dutin, C. J. Saraceno, M. Trant, O. H. Heckl, Y. Y. Wang, C. Schriber, F. Gerome, T. Südmeyer, F. Benabid, and U. Keller, "Beam delivery and pulse compression to sub-50 fs of a modelocked thin-disk laser in a gas-filled Kagome-type HC-PCF fiber," *Opt. Express* **21**, 4986–4994 (2013).

9. F. Guichard, A. Giree, Y. Zaouter, M. Hanna, G. Machinet, B. Debord, F. Gérôme, P. Dupriez, F. Druon, C. Hönninger, E. Mottay, F. Benabid, and P. Georges, "Nonlinear compression of high energy fiber amplifier pulses in air-filled hypocycloid-core Kagome fiber," *Opt. Express* **23**, 7416–7423 (2015).
10. V. Cardin, N. Thiré, S. Beaulieu, V. Wanie, F. Légaré, and B. E. Schmidt, "0.42 TW 2-cycle pulses at 1.8 μm via hollow-core fiber compression," *Appl. Phys. Lett.* **107**, 181101 (2015).
11. J. Schulte, T. Sartorius, J. Weitenberg, A. Vernaleken, and P. Russbueltdt, "Nonlinear pulse compression in a multi-pass cell," *Opt. Lett.* **41**, 4511–4514 (2016).
12. J. A. Valdmanis, R. L. Fork, and J. P. Gordon, "Generation of optical pulses as short as 27 femtoseconds directly from a laser balancing self-phase modulation, group-velocity dispersion, saturable absorption, and saturable gain," *Opt. Lett.* **10**, 131–133 (1985).
13. F. Salin, P. Grangier, G. Roger, and A. Brun, "Observation of high-order solitons directly produced by a femtosecond ring laser," *Phys. Rev. Lett.* **56**, 1132–1135 (1986).
14. J. Pouysegur, M. Delaigue, Y. Zaouter, C. Hönninger, E. Mottay, A. Jaffrès, P. Loiseau, B. Viana, P. Georges, and F. Druon, "Sub-100-fs Yb:CALGO nonlinear regenerative amplifier," *Opt. Lett.* **38**, 5180–5183 (2013).
15. M. Nurhuda, A. Suda, and K. Midorikawa, "Plasma-induced spectral broadening of high-energy ultrashort laser pulses in a helium-filled multiple-pass cell," *J. Opt. Soc. Am. B* **23**, 1946–1953 (2006).
16. D. Herriott, H. Kogelnik, and R. Kompfner, "Off-axis paths in spherical mirror interferometers," *Appl. Opt.* **3**, 523–526 (1964).
17. D. N. Papadopoulos, F. Friebe, A. Pellegrina, M. Hanna, P. Camy, J.-L. Doualan, R. Moncorgé, P. Georges, and F. Druon, "High repetition rate Yb:CaF₂ multipass amplifiers operating in the 100 mJ range," *IEEE J. Select. Top. Quantum. Electron.* **21**, 464–474 (2015).
18. R. Jung, J. Tümmeler, and I. Will, "Regenerative thin-disk amplifier for 300 mJ pulse energy," *Opt. Express* **24**, 883–887 (2016).
19. L. Lavenu, M. Natile, F. Guichard, Y. Zaouter, M. Hanna, E. Mottay, and P. Georges, "High-energy few-cycle Yb-doped fiber amplifier source based on a single nonlinear compression stage," *Opt. Express* **25**, 7530–7537 (2017).